

## SYNTHESIS AND CHARACTERIZATION OF AMORPHOUS ALLOY $\text{Co}_{69}\text{Nb}_{25}\text{B}_6$

Luciano Nascimento \*, Adriano Lima da Silva , Ana Cristina Figueiredo de Melo Costa 

*Laboratory of Synthesis of Ceramic Materials, Academic Unit of Materials Engineering,  
Federal University of Campina Grande, 882, Aprigio Veloso av., Bodocongó,  
Campina Grande– Paraiba 58429-900, Brazil  
\*e-mail: luciano.uepb@gmail.com*

**Abstract.** In this paper, amorphous alloy composition  $\text{Co}_{69}\text{Nb}_{25}\text{B}_6$  was prepared by high-energy ball milling which allows the formation of phases through solid state reaction. In addition, the effects of a 21:1 powder to ball mass ratio were used and the milling time during high energy milling was crucial for the formation of the amorphous and ferromagnetic phases. The characterization of the  $\text{Co}_{69}\text{Nb}_{25}\text{B}_6$  alloy was investigated by X-ray diffraction, scanning electron microscopy and hysteresis loops of alloy were measured with a VSM, and exhibited the typical soft magnetic character.

**Keywords:** amorphous alloy, high-energy ball milling, ferromagnetic phase.

*Received: 20 September 2022/ Revised final: 18 November 2022/ Accepted: 20 November 2022*

### Introduction

In 1960,  $\text{Au}_{75}\text{Si}_{25}$  was obtained as an amorphous alloy directly from the liquid state by a rapid-quenching technique. Amorphous alloys, also known as metallic glasses, are defined by a short-range ordered and a long-range disordered metastable structure [1]. The amorphous alloys exhibit high permeability, low core losses, high magnetic softness of low coercivity, high yield strength, high ductility, high corrosion resistance, and excellent catalytic performance in water treatments [2].

Many amorphous alloy systems based on Fe, Co, Nb, Zr, Ni, Ti and Pt are synthesized and studied [3]. The Co-based amorphous alloy is one of the most attractive systems due to its considerably low cost, superior mechanical properties (high strength and high hardness) and its high amorphous phase formation [4,5]. Amorphous phases in alloys can be well-defined metastable states, which can be created by reactions induced by thermal annealing [6]. This means that the amorphous phase is usually not the most stable phase. At low temperature, the crystalline phase is more stable; at high temperature, the liquid phase is more stable. However, amorphous phases can be observed and studied because their transformation into crystalline phases are very slow at room temperature.

As for Fe- and Co-based amorphous metal alloys, these materials have a pronounced soft

magnetic effect. These glasses have minimal hysteresis losses due to their narrow hysteresis. Various Fe- and Co-based amorphous alloys under the trademarks of METGLAS and VITROVAC were successfully developed with different performance conditions and displayed good ductility and excellent magnetic properties, and high amorphous-forming ability [7,8]. Different processing techniques have been developed to obtain amorphous alloys such as thermal spray, physical vapor deposition, chemical vapor deposition, melt-spinning and high-energy milling [9]. High energy milling (HEM) has proven to provide high consolidation of metal powders. The high-energy ball milling is a completely solid-state processing method that is not bound to phase diagrams and can produce many amorphous alloys, which cannot be produced by fast solidifying processing [10,11]. Among various amorphous alloys, there is a large supercooled liquid region of Eq.(1).

$$\Delta T = (T_x - T_g) \quad (1)$$

where,  $T_x$  - the crystallization start temperature of the first stage corresponding to the primary exothermic peak;  
 $T_g$  - glass transition temperature.

There is a correlation between the glass-forming ability and  $\Delta T$ . Since  $\Delta T$  is the difference between the crystallization and glass transition

temperatures, the alloy with good glass-forming ability should have some retardation force against crystallization [12,13]. Crystallization of amorphous alloys/bulk metallic glasses (BMGs) occurs as a second exothermic thermal effect, at slightly higher temperatures. Transmission electron microscopy was used to investigate the possibility of phase separation within the amorphous state at temperatures corresponding to lower DSC peaks. The objective of this work is to process the amorphous alloy, using the technique of solid-state reaction by high energy milling, which is one of the most widespread in the production of nanostructured powders, for scientific and commercial purposes.

### Experimental

The pure metallic powders of Co (99.99%, 60 $\mu$ m), Nb (99.99% 60 $\mu$ m) and B (99.9% 58 $\mu$ m) purchased from Sigma-Aldrich and Brazilian Metallurgy and Mining Company (BMMC), were weighed on a precision balance, Micronal B4000 with a resolution of 10<sup>-2</sup> g, obtaining a desired Co<sub>69</sub>Nb<sub>25</sub>B<sub>6</sub> composition, and were subjected to high-energy ball milling.

High energy grinding was performed using a planetary ball mill (Fritsch Pulverisette P5. 7) in hardened steel flasks using hardened steel balls (diameter: 10 mm), with disk rotation per minute and ball/powder weight ratio of 300 rpm and 20:1, respectively. Agglomeration and contamination were restricted using toluene (C<sub>7</sub>H<sub>8</sub>) as a process control agent (PCA, 50 mL, approximately one third of the vial volume to keep powders and balls fully immersed and promote efficient impact); and stearic acid (CH<sub>3</sub>(CH<sub>2</sub>)<sub>16</sub>COOH, 0.08% by weight) was added to reduce cold welding between metal powders. Mixing the mechanically bonded powders produced a totally amorphous structure with 10 hours of milling. The milling of the amorphous alloy Co<sub>69</sub>Nb<sub>25</sub>B<sub>6</sub> was carried out for a milling time of 10 hours. The desirable amorphous phase was obtained in 10 hours.

The analysis of the amorphous structure was performed by X-ray diffraction (XRD) with a BRUKER diffractometer, model D2 Phaser, a copper radiation (CuK $\alpha$ <sub>1</sub> = 1.54056 Å) at 40 kV and 30 mA), scanning in the region of 10° ≤ 2 $\theta$  ≤ 80°, with a speed of 0.016°/min and a time of 5 s.

The morphological aspect of the sample of amorphous alloy Co<sub>69</sub>Nb<sub>25</sub>B<sub>6</sub> powders was analysed by means of scanning electron microscopy in a VEGA3 equipment, TESCAN,

operating at 30 kV using a magnification of 1000x.

The high field magnetization curves were measured by a Microsense model EZ7 Vibrant Sample Magnetometer (VSM) subjected to magnetic fields up to 2.7 T (i.e., 27 kOe) and at the temperature in the range of 77 K to 1000 K. The field magnetization was parallel to the field direction of the sample to minimize the demagnetization effect. The magnetization curves were analysed by the least squares method. The coercive force H<sub>c</sub> of the rods was investigated using a coercimeter with a permalloy probe.

### Results and discussion

The technique, chosen to obtain the proposed amorphous alloy Co<sub>69</sub>Nb<sub>25</sub>B<sub>6</sub> allows us to evaluate the morphology of the particles with a milling time of 10 h, with disk rotation per minute and ball/powder weight ratio of 300 rpm and 20:1. The sample of Co<sub>69</sub>Nb<sub>25</sub>B<sub>6</sub> alloy in the amorphous state were characterized by XRD analysis, scanning electron microscope and magnetic measurements using a vibrating sample magnetometer (VSM), in order to verify phases and magnetic properties in the amorphous structure of the Co<sub>69</sub>Nb<sub>25</sub>B<sub>6</sub> alloy.

Figure 1 shows the X-ray diffractogram of the received amorphous alloy Co<sub>69</sub>Nb<sub>25</sub>B<sub>6</sub>. As can be seen inside the red circle, the amorphous structure can be recognized via the XRD pattern. The halo peak of Co<sub>69</sub>Nb<sub>25</sub>B<sub>6</sub> amorphous alloy lies between 35 to 50°. In general, the XRD patterns of Al<sub>87</sub>Ni<sub>8</sub>Gd<sub>5</sub> type amorphous alloys show a broad peak form (halo) centered at 42°, proving that the amorphous phase still exists after heat treatment [14].

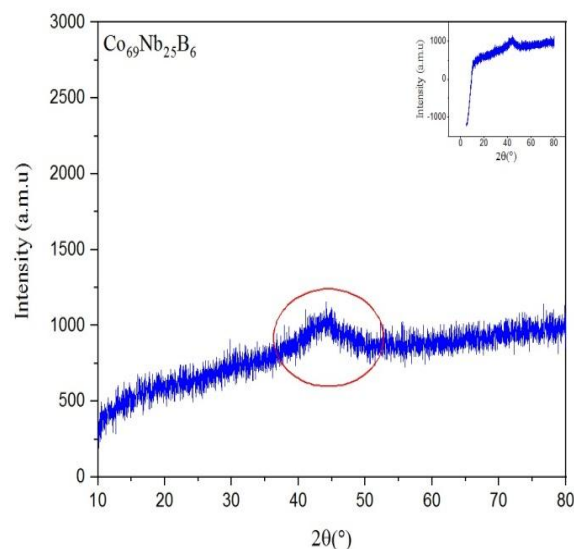
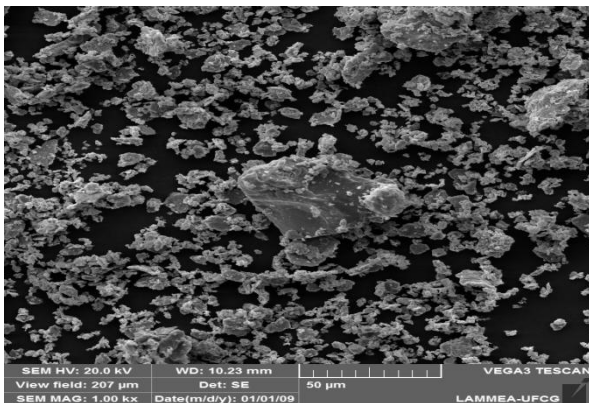


Figure 1. X-ray diffractogram of amorphous alloy Co<sub>69</sub>Nb<sub>25</sub>B<sub>6</sub>.

According to Figure 2, the microstructural morphology of the  $\text{Co}_{69}\text{Nb}_{25}\text{B}_6$  amorphous alloy powder are shown to be formed by irregular grains in the form of lamellar plates. As shown, with the extension of the milling time, the powders gradually transformed from the multilateral and irregular body, for lamellar plates morphology [15]. The large surface of the particles also gradually becomes more textured, indicating that the defect density of the powder increases with increasing milling time. Furthermore, the particle sizes of the powders gradually decrease and the number of powders with particle sizes of  $10\ \mu\text{m}$  gradually increases. During the ball milling process, particle flattening, cold welding, plastic deformation of welded particles and fracturing, all work together to reduce the scale of particles. Furthermore, many crystalline defects such as vacancies, dislocations and flattened subgrain contours are introduced, resulting in a substantial increase in the lattice distortion energy of the powder mixtures.



**Figure 2. SEM electron micrograph of the amorphous alloy  $\text{Co}_{69}\text{Nb}_{25}\text{B}_6$  in lamellar format.**

Figure 3 shows the hysteresis M-H loop of 0.16 T for the present amorphous alloy  $\text{Co}_{69}\text{Nb}_{25}\text{B}_6$ . Meanwhile, the  $H_c$  of this alloy was measured using a DC B-H loop tracer, and it showed a low  $H_c$  with the value of 23.9 kA/m. The behaviour of the magnetization curve starts at the origin, and represents a virgin magnetization curve. The  $M_s$  and  $H_c$  of the  $\text{Co}_{69}\text{Nb}_{25}\text{B}_6$  amorphous alloy are close to that of the amorphous alloy with similar composition produced using high-purity materials, indicating its good soft-magnetic properties.

It is shown that milled powders, particularly beyond 1 h, exhibit a relatively small curve area, which is an important characteristic of soft magnetic materials. Furthermore,  $\text{Co}_{69}\text{Nb}_{25}\text{B}_6$  alloy powders that are grounded for 10 hours and magnetize with applied field values, are around 300 Oe.

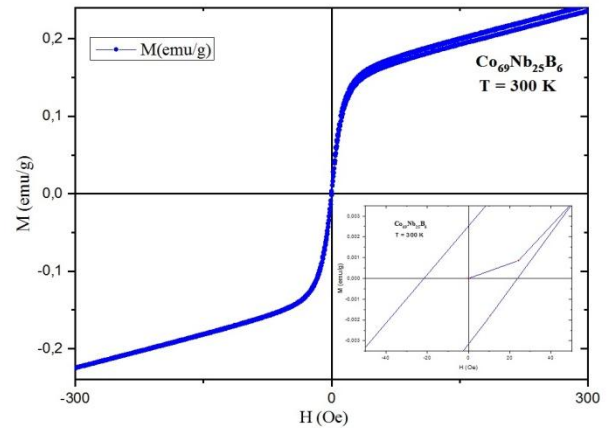


**Figure 3. Magnetization curve of the amorphous alloy  $\text{Co}_{69}\text{Nb}_{25}\text{B}_6$ .**

The  $M_s$  and  $H_c$  of the  $\text{Co}_{69}\text{Nb}_{25}\text{B}_6$  amorphous alloy are close to that of the amorphous alloy with similar composition produced using high-purity materials, indicating its good soft magnetic properties. Because amorphous metals lack periodic atomic arrangements and long-range homogeneous structure, the as cast samples exhibited good soft magnetic properties [16,17]. It is widely acknowledged that the saturation magnetization of amorphous alloys mainly depends on their components and high Nb and B content benefits the enhancement of high saturation magnetization. The high soft magnetic properties of this alloy come at the expense of a very low magnetic anisotropy constant. This is related to the lack of crystallographic anisotropy in amorphous alloy and magnetoelastic anisotropy in the Co-based alloy because of a close-to-zero magnetostriction constant. Once the spin-up band is saturated with more Co alloy, the spin-down band starts to fill up, resulting in a decrease in the concentration of unpaired electrons. Therefore, the effective magnetic moment of each magnetic atom increases and then decreases in the present Co-doped alloys. The composition rich in magnetostriction Co, becomes zero implying lower coercivity. The rapid initial suppression of M is attributed to the alloying of the non-magnetic element B with Nb and Co and the solid-state amorphization, according to XRD results [18]. It has been suggested that the addition of small fractions of metalloids with high electronegativity, such as B, is beneficial to increase the magnetization (M) between Co and Nb atoms [19]. In this case, the exchange integral is not very sensitive with variation of the Co-Co distance or 3d orbital radius of Co, according to the shape of the Bethe-slater curve [20]. In contrast, the addition of B is expected to slightly decrease the magnetization (M), due to chemical bonding and possible hybridization of orbitals for the B atom with 3d orbitals for Co and Nb atoms [21].

## Conclusions

The expanded single halo-shaped peak of the amorphous alloy  $\text{Co}_{69}\text{Nb}_{25}\text{B}_6$  is characteristic of the amorphous structures in these types of metallic systems.

SEM analysis shows a cluster of particles with platelet morphology and irregular lamellae with particle sizes of 10  $\mu\text{m}$  are formed due to the amorphization process present in the  $\text{Co}_{69}\text{Nb}_{25}\text{B}_6$  alloy.

The saturation magnetization of 0.15 emu/g for applied field values is 23.9 kA/m for the amorphous alloy  $\text{Co}_{69}\text{Nb}_{25}\text{B}_6$ , which depends on milling time, particle size and ferromagnetic behaviour. Metalloid fractions with high electronegativity in the  $\text{Co}_{69}\text{Nb}_{25}\text{B}_6$  alloy, such as B, are beneficial to increase the magnetization between Co and Nb atoms, enabling hybridization of orbitals for the B atom with 3d orbitals between atoms Co and Nb.

## Acknowledgments

The authors thank CAPES for the financial support and the research laboratories of LabSMaC and LaMMEA at the Federal University of Campina Grande.

## References

- Wang, J.; Ma, Y.; Guo, S.; Jiang, W.; Liu, Q. Effect of Sr on the microstructure and biodegradable behavior of Mg–Zn–Ca–Mn alloys for implant application. *Materials & Design*, 2018, 153, pp. 308–316. DOI: <https://doi.org/10.1016/j.matdes.2018.04.062>
- Li, Q.F.; Weng, H.R.; Suo, Z.Y.; Ren, Y.L.; Yuan, X.G.; Qiu, K.Q. Microstructure and mechanical properties of bulk Mg–Zn–Ca amorphous alloys and amorphous matrix composites. *Materials Science and Engineering: A*, 2008, 487(1-2), pp. 301–308. DOI: <https://doi.org/10.1016/j.msea.2007.10.027>
- Kumar, A.; Nayak, S.K.; Laha, T. Comparative study on wear and corrosion behavior of plasma sprayed  $\text{Fe}_{73}\text{Cr}_2\text{Si}_{11}\text{B}_{11}\text{C}_3$  and  $\text{Fe}_{63}\text{Cr}_9\text{P}_5\text{B}_{16}\text{C}_7$  metallic glass composite coatings. *Journal of Thermal Spray Technology*, 2022, 31, pp. 1–15. DOI: <https://doi.org/10.1007/s11666-021-01280-1>
- Zhao, J.; Gao, Q.; Wang, H.; Shu, F.; Zhao, H.; He, W.; Yu, Z. Microstructure and mechanical properties of Co-based alloy coatings fabricated by laser cladding and plasma arc spray welding. *Journal of Alloys and Compounds*, 785, 2019, pp. 846–854. DOI: <https://doi.org/10.1016/j.jallcom.2019.01.056>
- Zhou, Z.; Wei, Q.; Li, Q.; Jiang, B.; Chen, Y.; Sun, Y. Development of Co-based bulk metallic glasses as potential biomaterials. *Materials Science and Engineering: C*, 2016, 69, pp. 46–51. DOI: <https://doi.org/10.1016/j.msec.2016.05.025>
- Chen, J.; Zhao, G.; Zhang, Y.; Duan, S.; Matsuda, K.; Zou, Y. Metastable phase evolution and nanoindentation behavior of amorphous Ni–Cu–P coating during heat treatment process. *Journal of Alloys and Compounds*, 2019, 805, pp. 597–608. DOI: <https://doi.org/10.1016/j.jallcom.2019.07.068>
- Nykyruy, Y.; Mudry, S.; Shtablavyi, I.; Borisyuk, A.; Tsekhmister, Y.; Gnilitzkyi, I. Formation of laser-induced periodic surface structures on amorphous Fe- and Co-based alloys and its impact on magnetic properties. *Materials Chemistry and Physics*, 2022, 287, pp. 126317. DOI: <https://doi.org/10.1016/j.matchemphys.2022.126317>
- Li, T.H.; Liao, Y.C.; Song, S.M.; Jiang, Y.L.; Tsai, P.H.; Jang, J.S.C.; Huang, J.C. Significantly enhanced mechanical properties of ZrAlCo bulk amorphous alloy by microalloying with Ta. *Intermetallics*, 2018, 93, pp. 162–168. DOI: <https://doi.org/10.1016/j.intermet.2017.12.008>
- Xu, Y.; Zhou, S.; Liao, B.; Zhao, S.; Dai, X.; Chen, D. Effect of milling time on the microstructure and magnetic properties of amorphous  $\text{Ti}_{50}\text{Fe}_{50}$  alloys prepared by mechanical alloying. *Journal of Materials Research and Technology*, 2019, 8(5), pp. 3929–3935. DOI: <https://doi.org/10.1016/j.jmrt.2019.07.001>
- Révész, Á.; Kovács, Z. Severe plastic deformation of amorphous alloys. *Materials Transactions*, 2019, 60(7), pp. 1283–1293. DOI: <https://doi.org/10.2320/matertrans.MF201917>
- Sergiienko, R.A.; Shcheretskyi, O.A.; Zadorozhnyy, V.Yu.; Verkhovliuk, A.M.; Louzguine-Luzgin, D.V. Investigation of  $\text{Zr}_{55}\text{Cu}_{30}\text{Al}_{10}\text{Ni}_5$  bulk amorphous alloy crystallization. *Journal of Alloys and Compounds*, 2019, 791, pp. 477–482. DOI: <https://doi.org/10.1016/j.jallcom.2019.03.270>
- Abrosimova, G.E.; Aronin, A.S. Formation of metastable phases during crystallization of amorphous iron-based alloys. *Crystallography Reports*, 2020, 65(4), pp. 573–576. DOI: <https://doi.org/10.1134/S1063774520030037>
- Ibrahim, M.Z.; Sarhan, A.A.D.; Kuo, T.Y.; Hamdi, M.; Yusof, F.; Chien, C.S.; Chang, C.P.; Lee, T.M. Advancement of the artificial amorphous-crystalline structure of laser cladded FeCrMoCB on nickel-free stainless-steel for bone-implants. *Materials Chemistry and Physics*, 2019, 227, pp. 358–367. DOI: <https://doi.org/10.1016/j.matchemphys.2018.12.104>
- Abrosimova, G.E.; Aronin, A.S. Surface morphology of deformed amorphous-nanocrystalline materials and the formation of nanocrystals. *Journal of Surface Investigation: X-Ray, Synchrotron and Neutron Techniques*, 2018, 12(3), pp. 492–498. DOI: <https://doi.org/10.1134/S1027451018030023>
- Taghvaei, A.H.; Stoica, M.; Khoshkhoo, M.S.; Thomas, J.; Vaughan, G.; Janghorban, K.; Eckert, J. Microstructure and magnetic

- properties of amorphous/nanocrystalline  $\text{Co}_{40}\text{Fe}_{22}\text{Ta}_8\text{B}_{30}$  alloy produced by mechanical alloying. *Materials Chemistry and Physics*, 2012, 134(2-3), pp. 1214–1224. DOI: <https://doi.org/10.1016/j.matchemphys.2012.04.031>
16. Peng, K.; Tang, L.; Wu, Y. Evolution of microstructure and magnetic properties of  $\text{Fe}_{73.5}\text{Si}_{13.5}\text{B}_9\text{Nb}_3\text{Cu}_1$  amorphous alloy during ion bombardment process. *Journal of Magnetism and Magnetic Materials*, 2018, 460, pp. 297–301. DOI: <https://doi.org/10.1016/j.jmmm.2018.04.020>
  17. Li, X.; Wu, Y.; Yang, S.; Cha, X.; Shao, P.; Wang, L. Preparation and degradation property of magnetic FePBCSi amorphous alloy powder. *Journal of Non-Crystalline Solids*, 2019, 503-504, pp. 284–287. DOI: <https://doi.org/10.1016/j.jnoncrysol.2018.10.010>
  18. Masood, A.; Baghbaderani, H.A.; Ström, V.; Stamenov, P.; McCloskey, P.; Mathúna, C.Ó.; Kulkarni, S. Fabrication and soft magnetic properties of rapidly quenched Co-Fe-B-Si-Nb ultra-thin amorphous ribbons. *Journal of Magnetism and Magnetic Materials*, 2019, 483, pp. 54–58. DOI: <https://doi.org/10.1016/j.jmmm.2019.03.079>
  19. Zhu, M.; Zhang, M.; Yao, L.; Nan, R.; Jian, Z.; Chang, F. Effect of Mo substitution for Nb on the glass-forming ability, magnetic properties, and electrical resistivity in  $\text{Fe}_{80}(\text{Nb}_{1-x}\text{Mo}_x)_5\text{B}_{15}$  ( $x = 0-0.75$ ) amorphous ribbons. *Vacuum*, 2019, 163, pp. 368–372. DOI: <https://doi.org/10.1016/j.vacuum.2019.02.043>
  20. Fang, Y.N.; Hahn, H.; Kobe, S.; Witte, R.; Singh, S.P.; Feng, T.; Ghafari, M. Modifying the transition temperature,  $120 \text{ K} \leq T_c \leq 1150 \text{ K}$ , of amorphous  $\text{Fe}_{90-x}\text{Co}_x\text{Sc}_{10}$  with simultaneous alteration of fluctuation of exchange integral up to zero. *Scientific Reports*, 2019, 9(1), pp. 1–9. DOI: <https://doi.org/10.1038/s41598-018-36891-2>
  21. Gao, X.; Zhou, Y.; Cheng, Z.; Tan, Y.; Liu, S.; Shen, Z. Doping sp-hybridized B atoms in graphyne supported single cobalt atoms for hydrogen evolution electrocatalysis. *International Journal of Hydrogen Energy*, 2019, 44(50), pp. 27421–27428. DOI: <https://doi.org/10.1016/j.ijhydene.2019.08.195>